Investigation of Shock Compression in Toroidal Geometry in the High Voltage Belt Pinch

F. Söldner

IPP 1/162 June 1977

MAX-PLANCK-INSTITUT FÜR PLASMAPHYSIK

8046 GARCHING BEI MÜNCHEN

MAX-PLANCK-INSTITUT FÜR PLASMAPHYSIK

GARCHING BEI MÜNCHEN

Investigation of Shock Compression in Toroidal Geometry in the High Voltage Belt Pinch

F. Söldner

IPP 1/162 June 1977

Die nachstehende Arbeit wurde im Rahmen des Vertrages zwischen dem Max-Planck-Institut für Plasmaphysik und der Europäischen Atomgemeinschaft über die Zusammenarbeit auf dem Gebiete der Plasmaphysik durchgeführt.

IPP 1/162 F. Söldner Investigation of Shock Compression in Toroidal Geometry in the High Voltage Belt Pinch

Abstract

Fast magnetic compression is investigated in the High Voltage Belt Pinch at two initial densities $n_{eo} = 3 \times 10^{13}$ cm^{-3} and $n_{eo} = 7 \times 10^{13}$ cm^{-3}. At the lower density the electrons are heated to 3 keV in the piston region, the ions trapped in the piston obtaining an energy of 0.7 keV. A third of the ions are reflected off the piston attaining an energy of 2.5 keV. At the higher initial density a central $\beta = 1$ plasma is formed. Electrons are heated to 1 keV in the sheath, the piston ions obtaining an energy of 0.4 keV. The degree of ion reflection is 60 %. Ion acoustic turbulence in both cases dominates the implosion phase and gives rise to the anomalous field diffusion and electron heating observed. Steep electron density and temperature gradients decisively enhance the effective drift velocity for wave growth. The experimental results are compared with numerical calculations using a hybrid code which includes anomalous transport. Scaling studies with the hybrid code in a wider density range show in agreement with the experiment increasing efficiency of shock heating for higher initial densities due to increasing ion reflection.

Index

1. Introduction

Fast magnetic compression is the most efficient method of producing weakly compressed high temperature plasmas, which are required in two important high-ß confinement systems. In the high-ß stellarator a small compression ratio and a high ß-value are essential for the effectiveness of the wall stabilization of long wavelength MHD modes /1/. On the other hand, in the belt pinch highly elongated equilibria can be achieved only if the radial compression ratio is small /2/. Shock compression has been closely investigated for many years in linear theta pinches /3 - 6/. End losses, however, feature prominently in linear devices, especially at low densities. The electron temperature is already reduced by electron heat conduction to the ends during compression. Eliminating end losses should therefore lead to higher electron temperatures. This might change the physical processes during the compression phase, e.g. piston formation, excitation of micro-instabilities and anomalous transport.

We therefore studied fast magnetic compression in toroidal geometry, continuing our previous work on linear devices /7, 8/. The experiments were performed in the Garching High Voltage Belt Pinch. This is a shock heated high-ß tokamak with highly elongated plasma cross-section. In order to attain high plasma temperatures by shock heating, it is necessary to apply high circumference voltages to the compression coil since the energy input to the plasma is proportional to the electric field strength at the plasma boundary. With a circumference voltage of 250 kV ion temperatures in the keV range can be attained at initial densities of a few times 10^{13} cm^{-3}.

In this paper fast magnetic compression is studied in the density regime $10^{13} - 10^{14}$ cm^{-3}. The development of the shock structure and the electron and ion heating mechanisms are analyzed. The experimental results are compared with plasma simulation calculations using a fluid-particle hybrid code. Parameter studies are conducted with the hybrid code to investigate the scaling of the electron and ion heating in a wider density range. The critical density below which compression heating becomes ineffective is determined. Towards higher densities the efficiency of the shock heating improves. An increasingly larger part of the energy is transferred to the ions owing to increasing reflection of the ions from the magnetic piston.

II. Experimental Set-up

1. Coil System

The coil system of the High Voltage Belt Pinch consists of two concentric coils each assembled from 36 helically wound single conductors (Fig. 1). The helical conductors are connected in parallel by means of circular collector plates. The top and bottom collector plates are powered in series. The entire helical coil is equivalent to a system of three coils arranged in series: a toroidal theta pinch coil which generates the compressing toroidal magnetic field, a ring-shaped coil inside and a ring-shaped coil outside the toroidal plasma belt. The latter two coils induce a toroidal plasma current. The ratio of the poloidal to the toroidal plasma current is determined by the pitch of the helix. The pitch of the inner coil is 64°, the pitch of the outer coil 43°. The pitch was chosen so that the plasma is compressed to the equilibrium position. For this purpose the centre of mass of the plasma belt has to be conserved during compression, and the same momentum has to be transferred to the inner and to the outer plasma surfaces. By means of an additional conductor outside the outer coil it is possible to control the amplitude and the time evolution of the magnetic fields.
The influence of a passive external short-circuit ring and an actively programmed external vertical field on the behaviour of the preionization plasma was investigated. Additional fields are not required for the main discharge till crowbar operation is initiated after the compression phase.

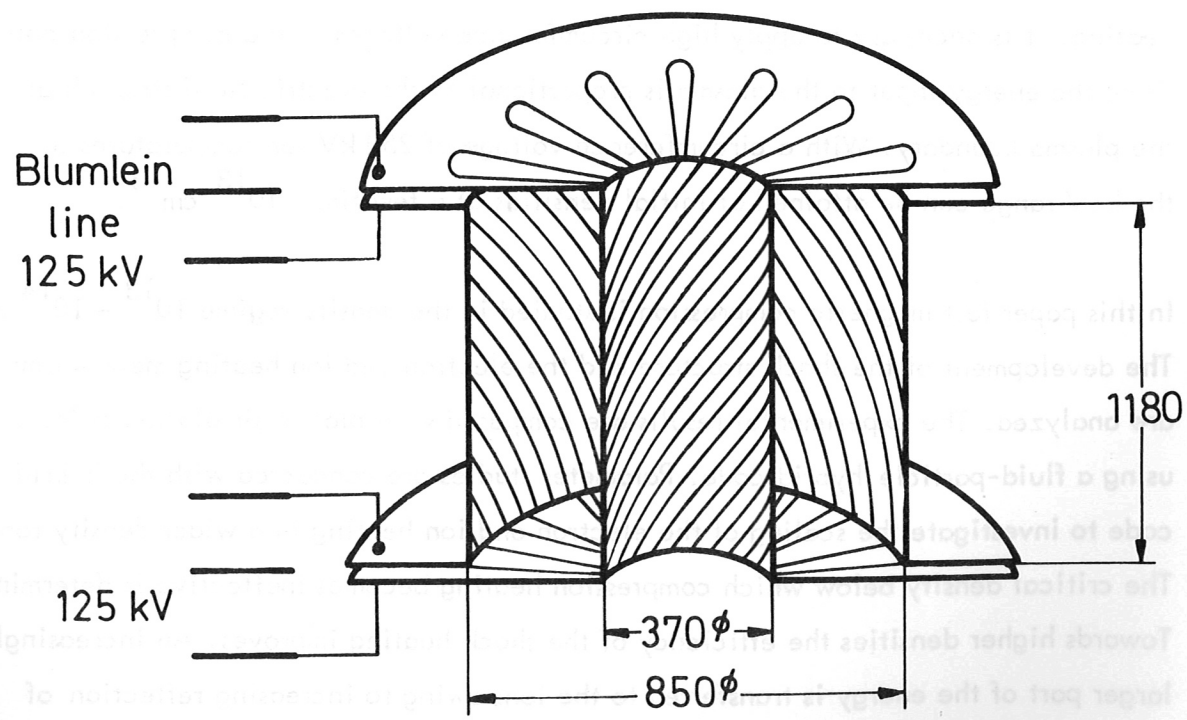

Fig. 1 Schematic drawing of the coil system of the High Voltage Belt-Pinch

2. Preionization

The initial plasma for the fast magnetic compression is produced in two stages: A high-frequency pulse (ν = 80 MHz) capacitively coupled to the coil system is followed by a subsequent ringing toroidal discharge (ν = 20 kHz) which leads to ionization of the neutral gas filling. The preionization bank is.decoupled from the main bank by inserting saturable iron core inductances into the predischarge circuit. The preionization was investigated by measuring the magnetic field profiles with probes, and the time variation of the radial electron density profiles by laser light scattering /9/. At a filling pressure of 2 mtorr deuterium the degree of ionization is about 50 % with radially uniform density distribution after two half-cycles of the predischarge.

3. High Voltage Discharge

Fast magnetic compression requires a fast rising magnetic field, which is generated by means of high circumference voltages at the coil. Blumlein lines are therefore used as low-inductance energy storage system. They are charged by three-stage Marx generators in pulsed operation (Fig. 2). The belt pinch coil is double fed by the Blumlein lines in order to double the circumference voltage at the coil. The data of the coil and electric circuits are given in Table 1.

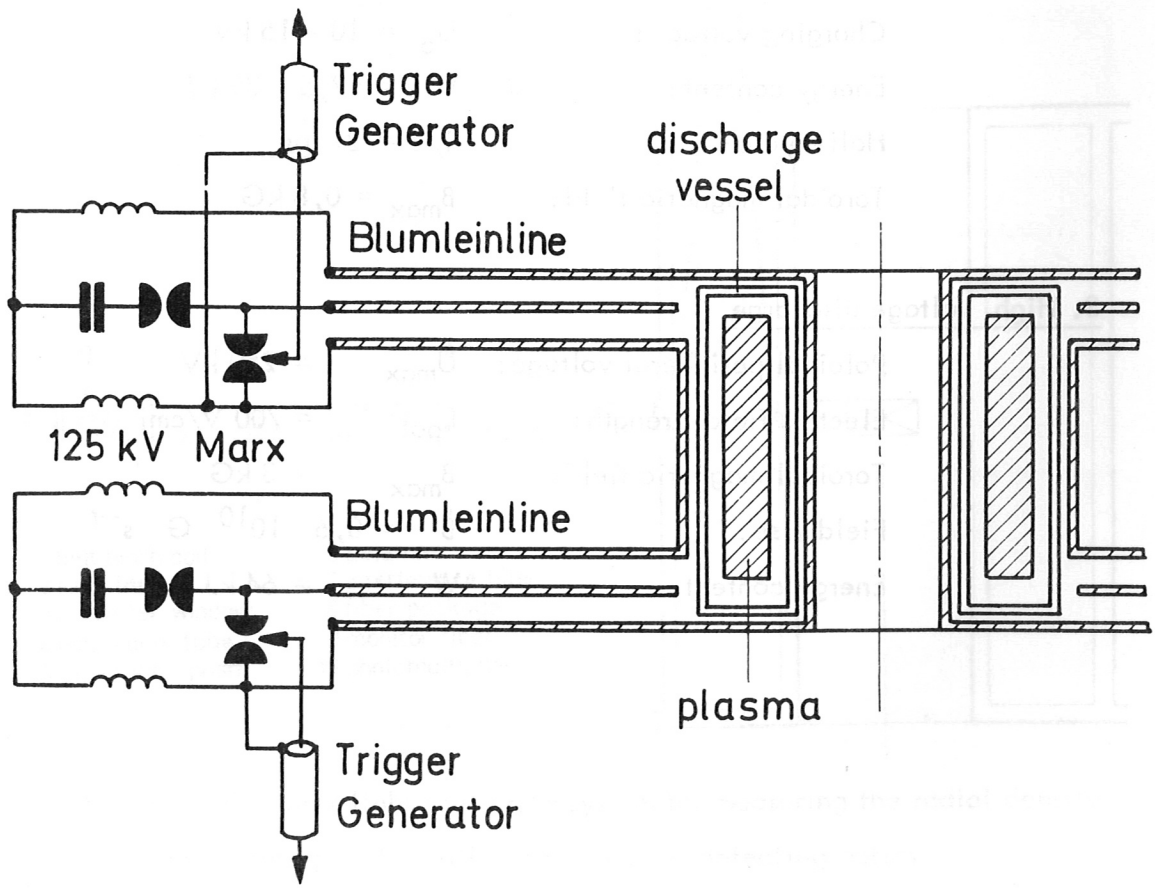

Fig. 2 Electric circuit of the high voltage discharge

Table 1: Technical data of the High Voltage Belt Pinch

Coil	Double fed, inner and outer coils helically wound	
	Pitch of inner coil: 64°	
	Pitch of outer coil: 43°	
	h	= 118 cm
	$\emptyset_a$	= 85 cm
	$\emptyset_i$	= 37 cm
1. High-frequency predischarge		
	Charging voltage:	U = 30 kV
	Energy content:	W = 50 J
	Discharge frequency	ν = 80 MHz
	Pulse length:	τ = 6 μs
2. Preionization		
	2-stage Marx circuits	
	Charging voltage:	U_o = 10 - 15 kV
	Energy content:	W = 17,5 - 39 kJ
	Half-cycle:	T/2 = 21 μs
	Toroidal magnetic field:	B_{max} = 0,8 kG
3. High voltage discharge		
	Poloidal peripheral voltage:	U_{max} = 250 kV
	Electric field strength:	E_{pol} = 700 V/cm
	Toroidal magnetic field:	B_{max} = 3 kG
	Field rise:	$\dot{B}$ = 0,6 10^{10} G s^{-1}
	Energy content:	W = 64 kJ

III. Diagnostics

A multichannel laser light scattering system is used for measuring the radial electron density and temperature profiles (Fig. 3). A Q-switched ruby laser irradiates the plasma in the midplane of the discharge vessel in the radial direction. The laser beam is focussed with small aperture into the plasma, where it retains an almost constant diameter of 5 mm. The light scattered at 90° by the electrons is imaged on a fibre-glass bundle consisting of 10 light pipes. Each channel is assigned to a scattering volume 2 cm in length. This allows radially resolved observation of the entire scattering region between the inner and outer vessel walls with one laser shot. Serious difficulties arose from the compact toroidal geometry since the laser beam has to be absorbed in the centre of the torus at a short distance from the plasma. Nevertheless the stray light was finally reduced to the level of Thomson scattering signals from electrons with a density of 10^{13} cm^{-3} /9/. Absolute density measurements are thus possible. To determine the electron temperature from the width of the scattering spectrum, interference filters with various bandwidths were inserted in the observation path. For most of the measurements, however, a 9-channel grating polychromator with a dispersion of 105 Å /channel was used. The entrance light pipe is successively connected to each of the radial channels.

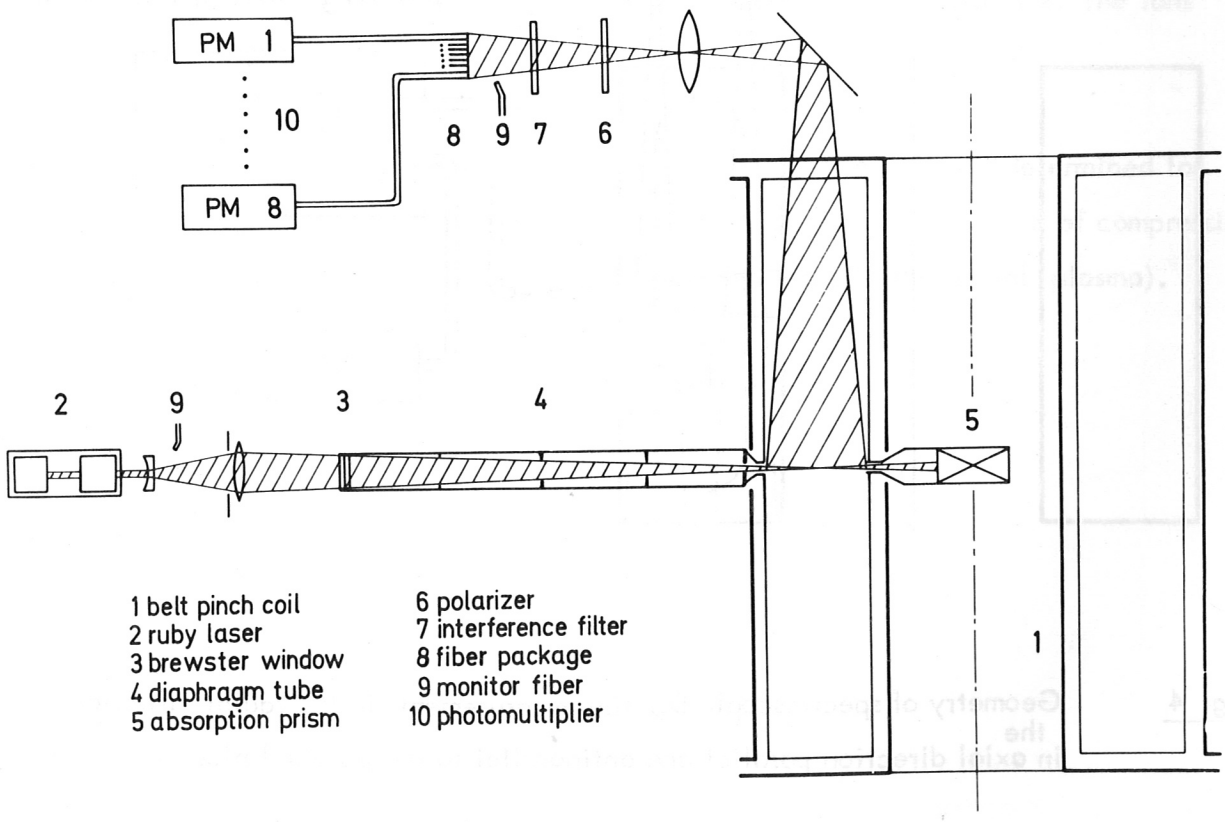

Fig. 3 Set-up of the laser light scattering system for measuring the radial density and temperature profiles with multi-channel detecting optics

The D_α line emission (λ = 6561 Å) is measured with a 10-channel grating polychromator (dispersion: 1.5 Å/ channel). It was carefully assembled for a high contrast: $1 : 5 \times 10^{-3} : 10^{-3}$ for 3 neighbouring channels. Spectroscopic measurements are made in the radial direction and in the poloidal direction parallel and antiparallel to the diamagnetic plasma current (Fig. 4). An O II line (λ = 4416 Å) is recorded as a monitor for the oxygen content in the plasma. For absolute calibration of the O II line emission small defined quantities of oxygen are added to the plasma and then the intensity of the O II line is observed. Extrapolation to zero oxygen additive yields the degree of oxygen impurity in the plasma.

The neutron flux from fusion collisions between deuterons is detected with a fast plastic scintillator. Fast multiple probes are used to trace the time evolution of the magnetic field profiles. The radial and axial motions of the plasma are observed with image converter cameras.

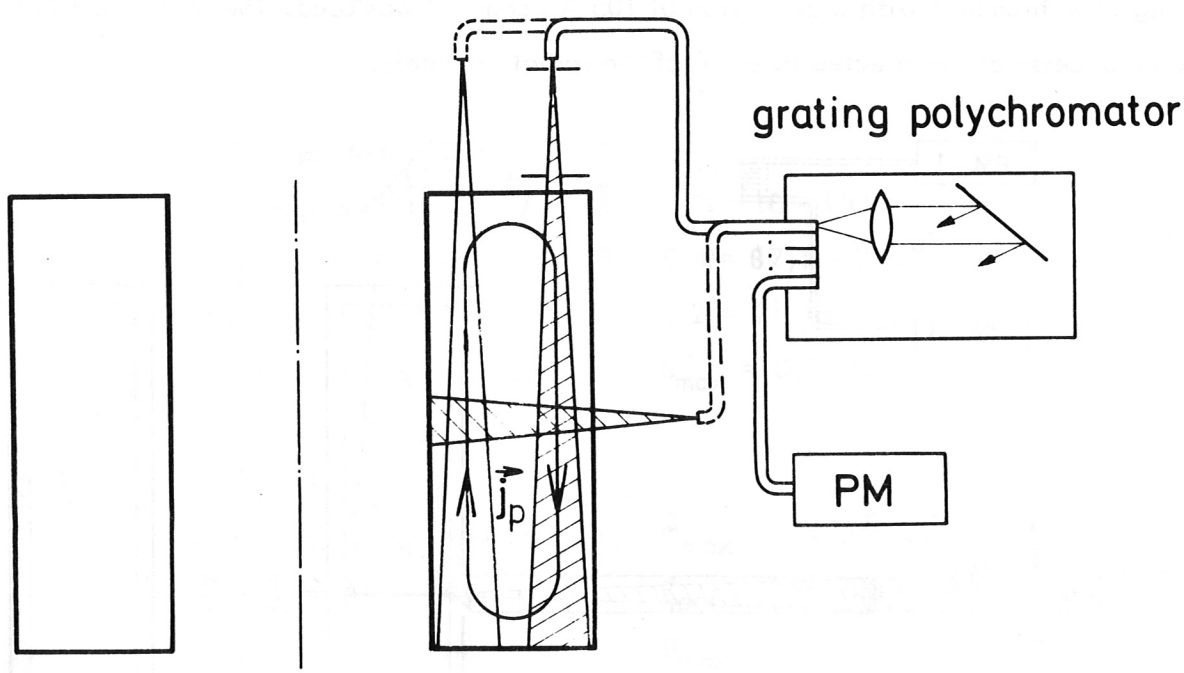

Fig. 4 Geometry of spectroscopic D_α line measurements in the radial direction and the in axial direction parallel and antiparallel to the poloidal plasma current

IV . Fast Magnetic Compression

The fast magnetic compression was investigated in the High Voltage Belt-Pinch for deuterium with initial densities $n_{eo} = 10^{13} - 10^{14}$ cm^{-3}. Two cases with $n_{eo} = 3\times10^{13}$ cm^{-3} and $n_{eo} = 7\times10^{13}$ cm^{-3} are studied in detail and compared.

1. Magnetic Field Profiles

At an initial density of $n_{eo} = 3\times10^{13}$ cm^{-3} the magnetic field penetrates the entire plasma (Fig. 5a). The compression time determined from the diamagnetic signal is about 400 ns. From the velocity of the magnetic piston an energy of 700 eV is derived for the ions collected in the piston. The same value is obtained from the radial velocity of the luminous front in streak pictures. The ß-value averaged over the plasma cross-section (ß = plasma pressure/pressure of the external magnetic field) is 0.4 after compression. The compression ratio (coil diameter/half-width of the plasma pressure) amounts to 3.5.

At the higher initial density $n_{eo} = 7\times10^{13}$ cm^{-3} the magnetic piston is slowed down by the gas kinetic pressure of the compressed plasma and is stopped at a third of the initial plasma diameter at the compression time of about 500 ns (Fig. 5b). A central ß = 1 plasma is formed. The mean ß-value obtained is 0.8. The final compression ratio is 2. The ions collected in the piston gain an energy of 400 eV.

From the radial magnetic field profiles the width of the magnetic piston is determined for both initial densities (Fig. 6). The width of the compression sheath at the end of compression is of the order 0.5 c/ω_{pio} (ω_{pio} = ion plasma frequency in the initial plasma).

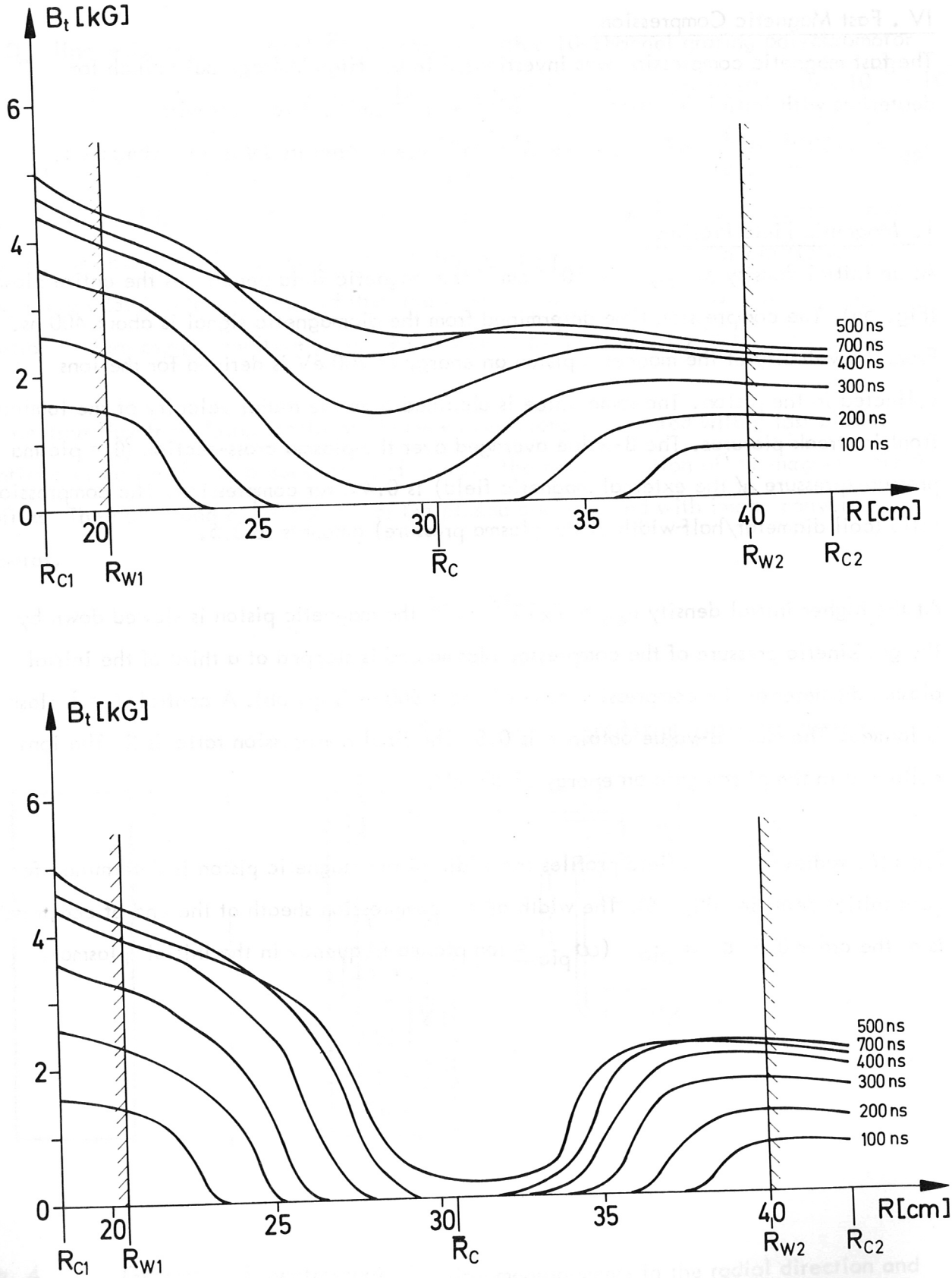

Fig. 5 Time evolution of the radial magnetic field profiles during shock compression of deuterium with an initial density of

a) $n_{eo} = 3 \times 10^{13}$ cm^{-3},

b) $n_{eo} = 7 \times 10^{13}$ cm^{-3}, R_{w1}, R_{w2}: radii of the discharge vessel, R_{c1}, R_{c2}: radii of the coil, $\bar{R}_c = (R_{c1} + R_{c2})/2$

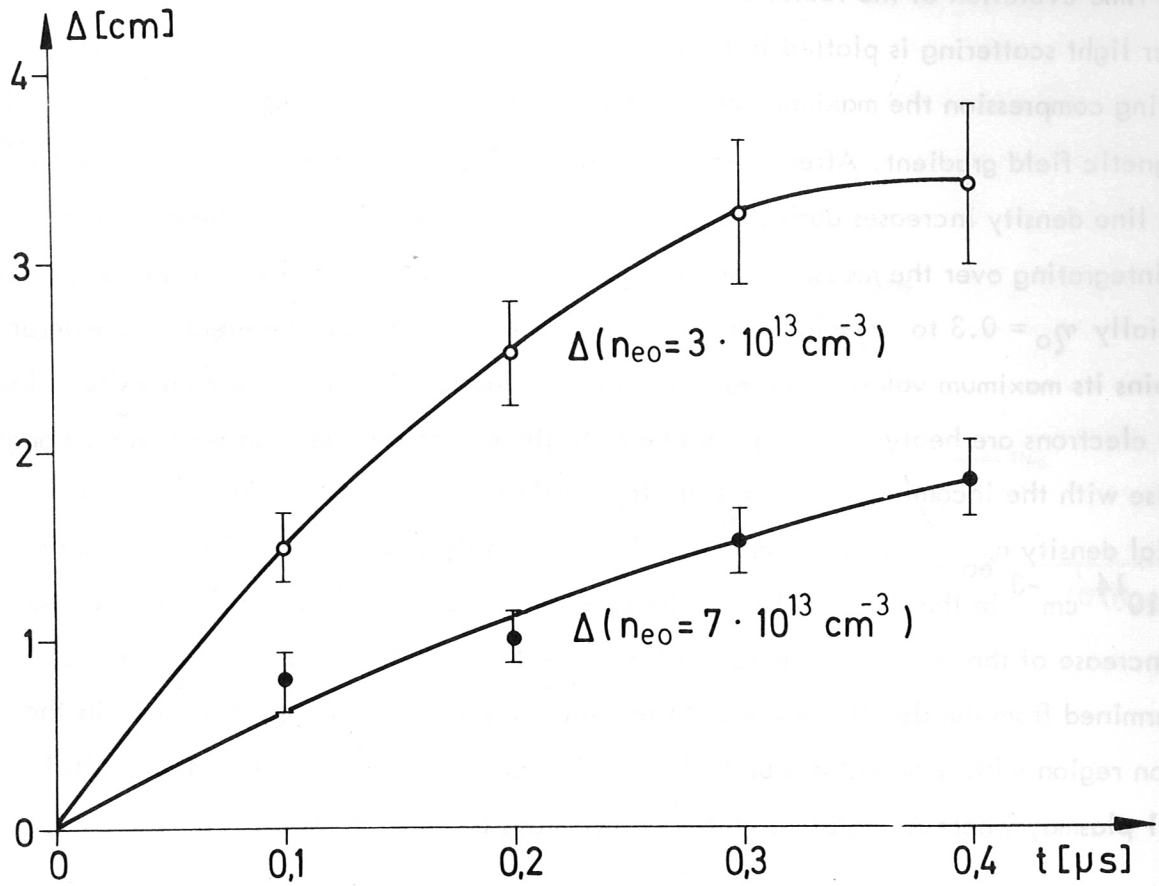

Fig. 6 Time history of the sheath width Δ of the magnetic piston

2. Radial Electron Density and Temperature Profiles

The time evolution of the radial electron density and temperature profiles measured by laser light scattering is plotted in Fig. 7 for the initial density $n_{eo} = 3 \times 10^{13}$ cm^{-3}. During compression the maximum of the electron density is in the region of the steepest magnetic field gradient. After compression the density rises in the centre to 1.5×10^{14} cm^{-3}. The line density increases during the implosion owing to ionization of the neutral background. By integrating over the measured density profiles an increase of the ionization degree from initially $\eta_o = 0.3$ to $\eta \approx 0.5$ after compression is determined. The electron temperature attains its maximum value in the rear part of the piston, where the plasma density is low. The electrons are heated there up to 3 keV. In the centre the electron temperature begins to rise with the incoming magnetic field to 1 keV at implosion time. At the higher initial density $n_{eo} = 7 \times 10^{13}$ cm^{-3} the electron density reaches a maximum value of 3×10^{14} cm^{-3} in the centre (Fig. 8). Ionization of the neutral gas background causes an increase of the degree of ionization from $\eta_o = 0.55$ to $\eta = 0.9$ at t = 600 ns as determined from the density profiles. Strong electron heating is observed again in the piston region with temperatures up to 1 keV. The electron temperature in the central $\beta = 1$ plasma, where no poloidal current flow, stays low ($T_e \leq 50$ eV).

Steep electron temperature gradients persist during compression at both initial densities. This might be due to limitation of the radial heat conduction by a small bias field ($B_o \approx 100$ G) remaining from the preionization discharge.
The electron cyclotron frequency according to the bias field is much larger than the collision frequency for heat conduction $\omega_{ge} >> \nu_{ee}$. An increase of the electron temperature in front of the piston even leads to self-limitation of the radial heat conduction because the conductivity $\kappa_\perp$ is proportional to ν_{ee} : $\kappa_\perp \sim \nu_{ee}$, and the collision frequency drops with rising electron temperature: $\nu_{ee} \sim T_e^{-3/2}$. This results in heat stagnation in the foot of the magnetic piston.

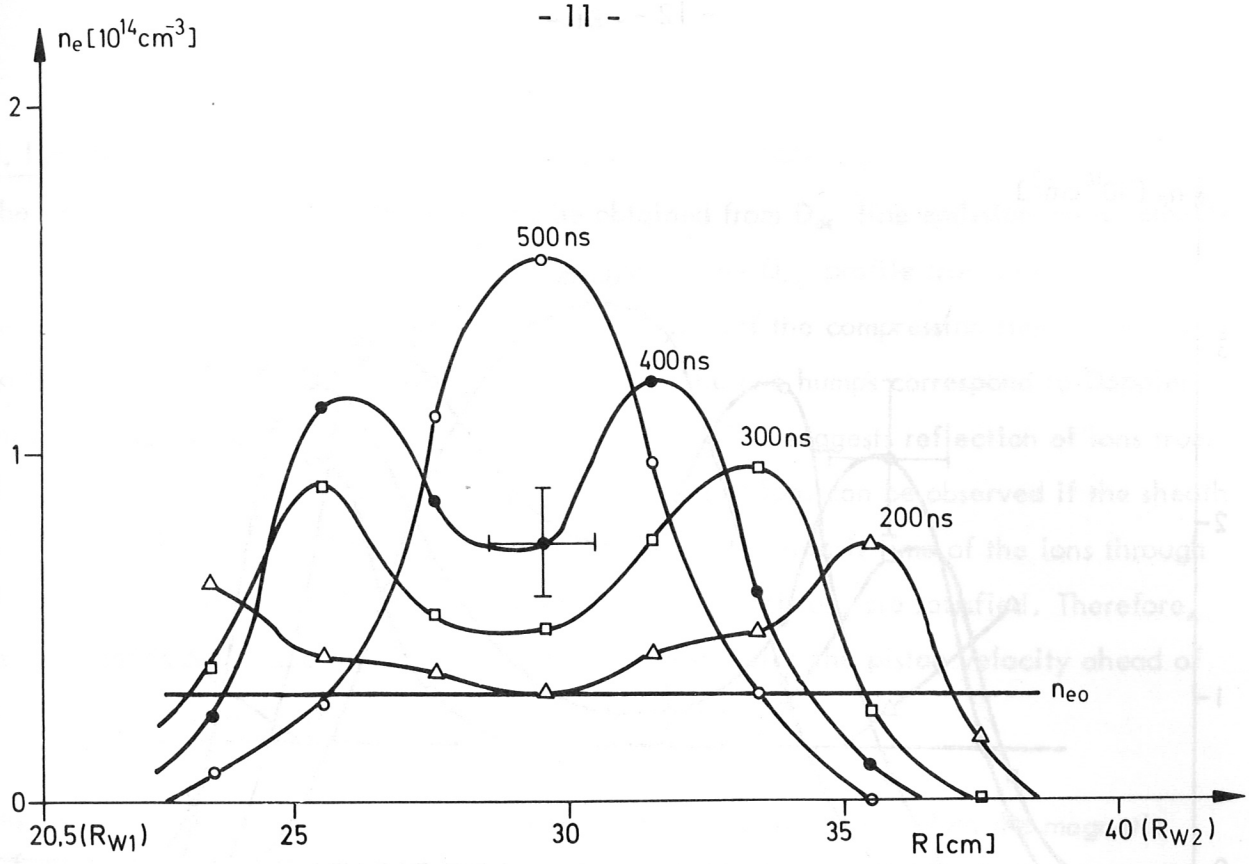

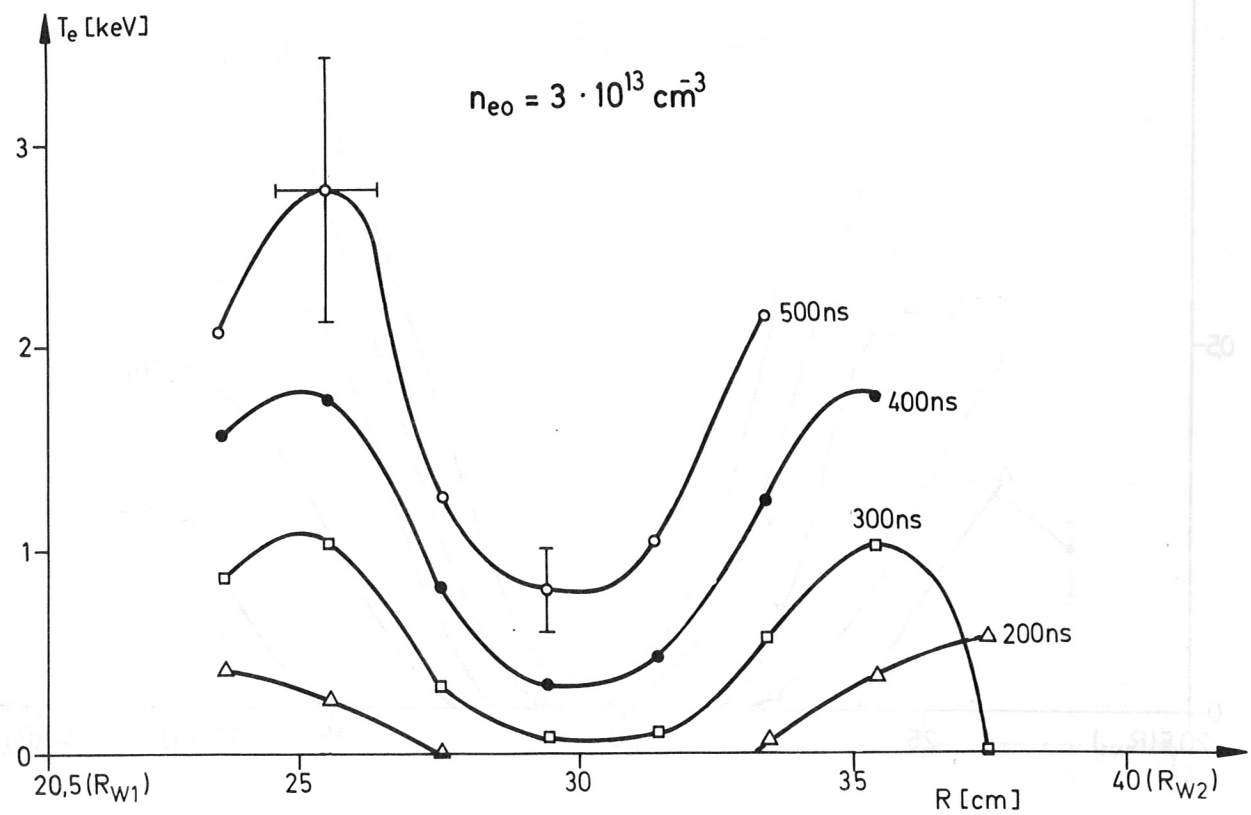

Fig. 7 Time evolution of the radial electron density and temperature profiles at the initial density $n_{eo} = 3 \times 10^{13}$ cm^{-3}

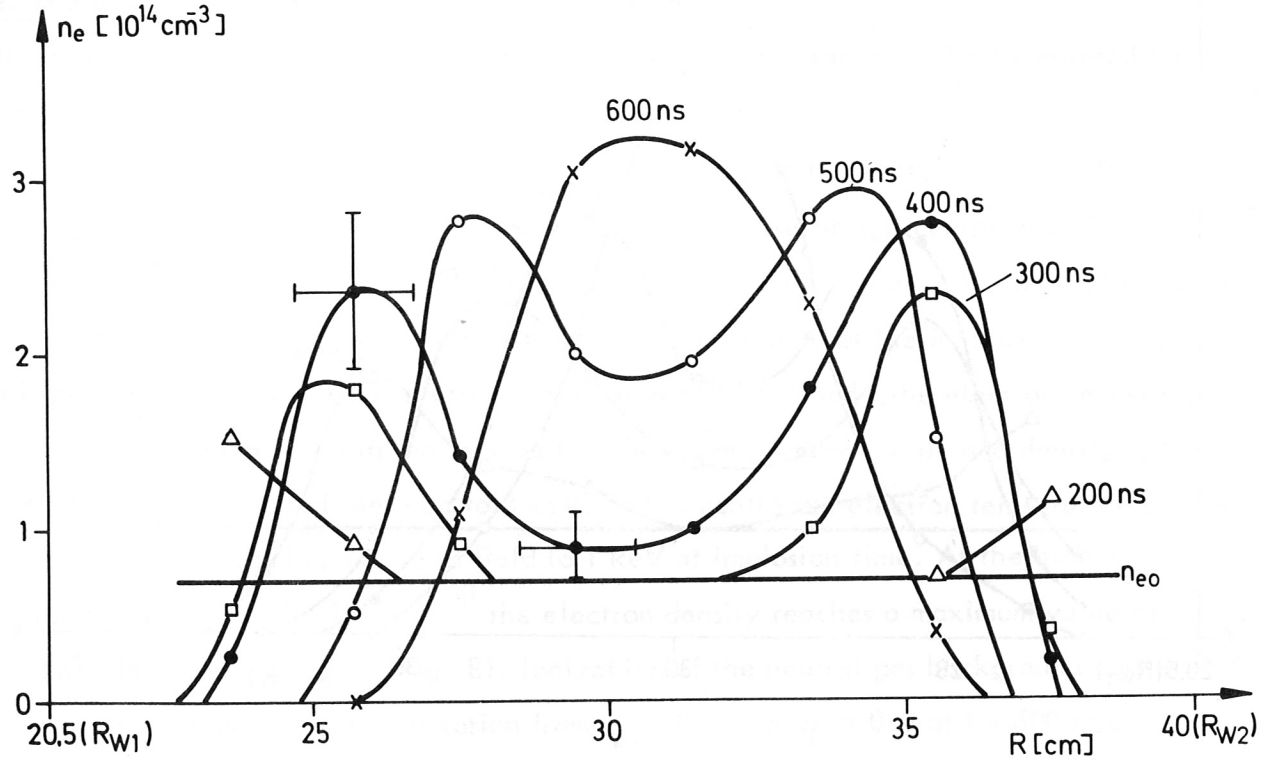

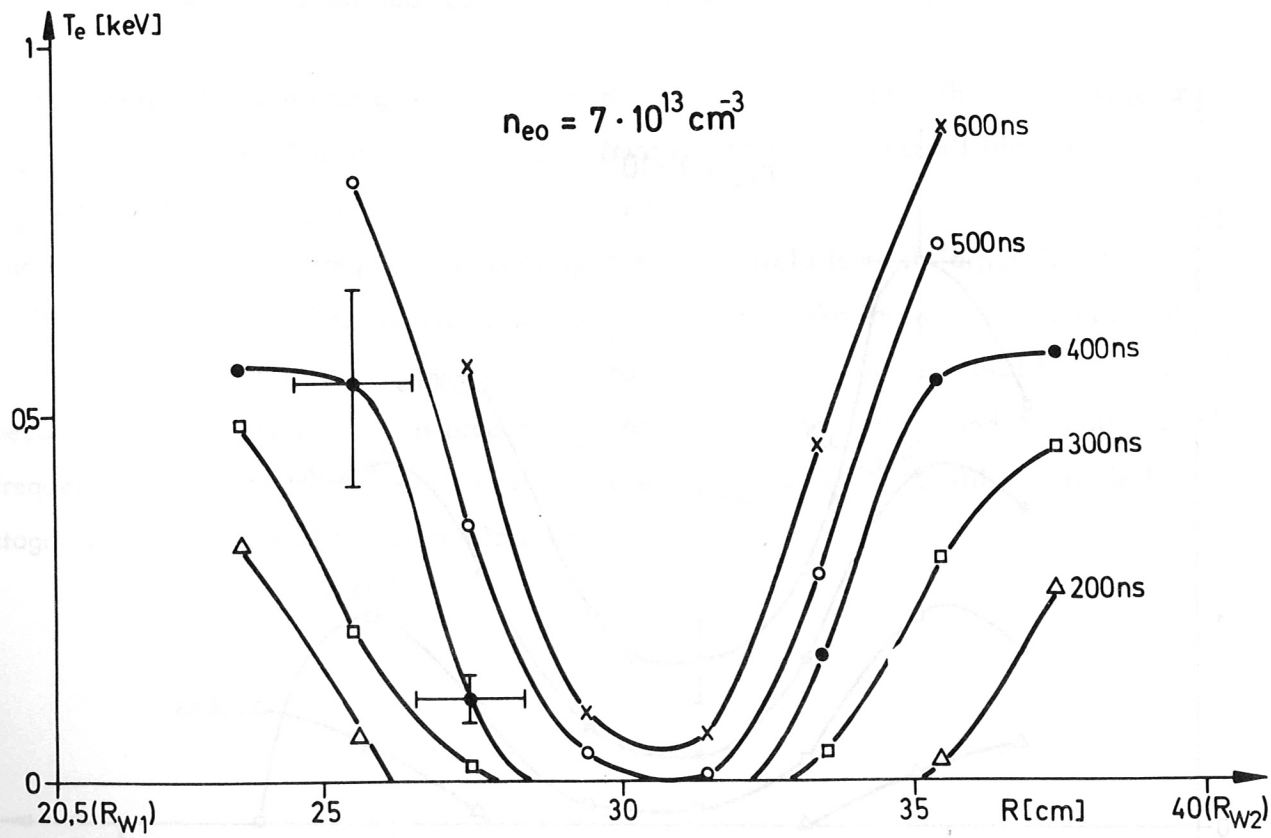

Fig. 8 Time evolution of the radial electron density and temperature profiles at the initial density $n_{eo} = 7 \times 10^{13}$ cm^{-3}

3. Ion Heating

The velocity distribution of the ions may be obtained from D_α line emission measurements due to charge exchange between ions and neutrals. The D_α profile from radial measurements is given in Fig. 9 for $n_{eo} = 7 \times 10^{13}$ cm^{-3} at half the compression time. The central part of the profile is due to excited atoms at rest. The two humps correspond to Doppler shifts with once and with double the piston velocity. This suggests reflection of ions from the potential jump across the shock layer. Reflection of ions can be observed if the sheath width is smaller than half the compression length and the transit time of the ions through the piston is shorter than the compression time. Both conditions are satisfied. Therefore, reflected ions can leave the sheath and proceed with twice the piston velocity ahead of the ions trapped in the piston.

The reflected ions cause an early rise of the neutron flux at a time when the magnetic piston has travelled half the compression length and the piston ions are not yet colliding (Fig. 10). The neutrons emitted at this time from the plasma arise from fusion collisions

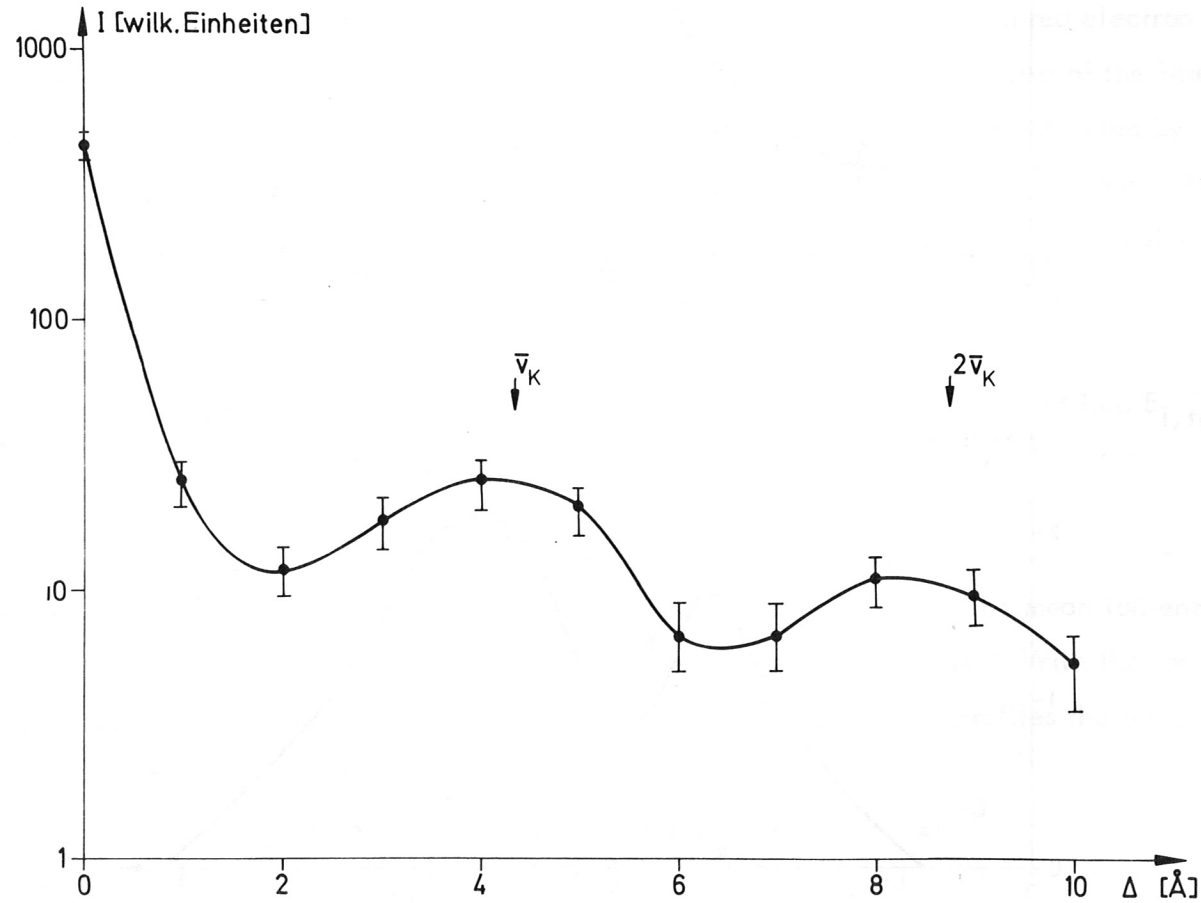

Fig. 9 D_α line profile, observed in the radial direction at $t = 0.3$ μs for $n_{eo} = 7 \times 10^{13}$ cm^{-3}

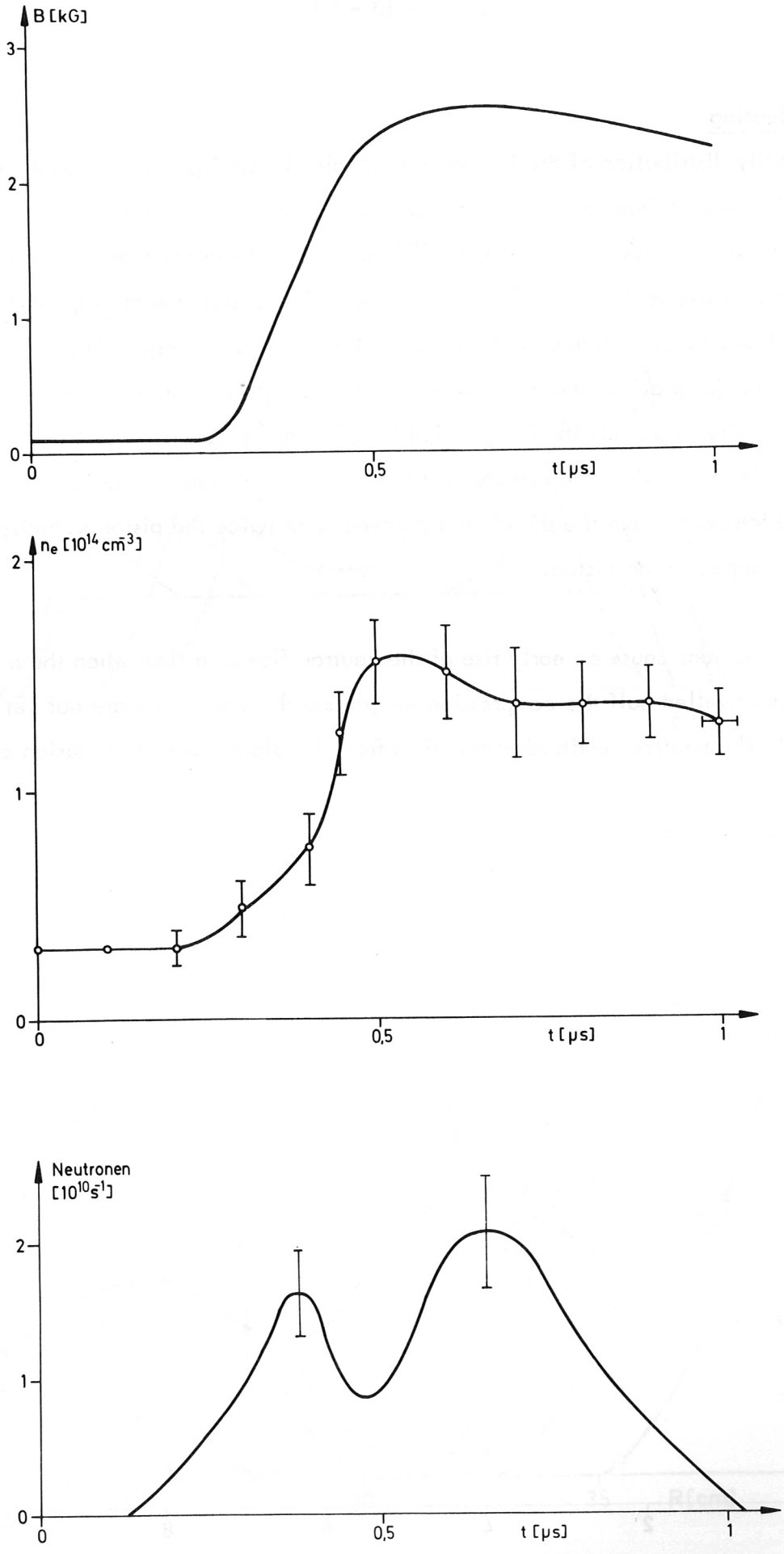

Fig. 10 Time histories of the toroidal magnetic field and electron density at R = 29.5 cm and the neutron flux for $n_{eo} = 3 \times 10^{13}$ cm^{-3}

between the reflected ions which already meet in the centre after about half the compression time. The first maximum of the neutron rate occurs when the reflected ions hit the piston again. The subsequent drop of the neutron flux might be due to a decrease of reflected ions colliding with piston ions. A second bouncing of the ions from the piston causes another rise of the neutron flux. The neutrons observed predominantly originate from collisions with reflected ions because the rate coefficient σv for neutron production in this energy range is proportional to the fourth power of the relative energy between the colliding particles and therefore

$$\langle \sigma v \rangle_{\text{neutron}} \sim v_i^8$$

with v_i = mean relative velocity between the ions colliding. From the neutron rate a mean energy of 2.5 keV is determined for the reflected ions at $n_{eo} = 3 \times 10^{13}$ cm^{-3}, assuming monoenergetic ion distribution. This energy corresponds to about four times the energy of the piston ions obtained from magnetic field profiles and D_α measurements.

The reflected ions give rise to an increase of the electron density in front of the magnetic piston while maintaining the quasineutrality of the plasma. From the measured electron density profiles the degree of ion reflection is determined by taking the ratio of the line density increase before the position of the piston to the total line density collected by the piston. The position of the piston is taken to be the location of the steepest magnetic field gradient. The reflection degree increases during compression and reaches a value of 0.3 for $n_{eo} = 3 \times 10^{13}$ cm^{-3} at implosion time and 0.6 for $n_{eo} = 7 \times 10^{13}$ cm^{-3}.

Mean ion energies $\bar{E}_i$ are calculated by averaging the energies of the trapped ions $E_{i,tr}$ and of the reflected ions $E_{i,refl}$:

$$\bar{E}_i = \alpha E_{i,refl.} + (1 - \alpha) E_{i,tr}$$

where α is the degree of ion reflection. For $n_{eo} = 3 \times 10^{13}$ cm^{-3} the mean ion energy amounts to $\bar{E}_i \approx 1.3$ keV, for $n_{eo} = 7 \times 10^{13}$ cm^{-3} to $\bar{E}_i \approx 1$ keV. With the radically averaged electron densities $\bar{n}_e$ determined from the measured profiles the ion energy densities ε_i are calculated at implosion time:

$$\varepsilon_i = \bar{n}_e \bar{E}_i = \begin{cases} 0.65 \times 10^{17} \text{ eV cm}^{-3} & \text{for } n_{eo} = 3 \times 10^{13} \text{ cm}^{-3} \\ 1.1 \times 10^{17} \text{ eV cm}^{-3} & \text{for } n_{eo} = 7 \times 10^{13} \text{ cm}^{-3} \end{cases}$$

The ion energy density is higher for the higher initial density owing to the larger degree of ion reflection. Accordingly, the efficiency of shock heating increases with increasing initial density in the range investigated as a result of stronger ion heating by ion reflection.

D_α line emission in the poloidal direction (see Fig. 4) reveals a two-temperature ion velocity distribution (Fig. 11). The red wing of the profile is enhanced owing to high energy ions flowing in the direction of the relative electron-ion drift velocity. Measurements counter to the drift confirm this feature. The blue wing of the spectrum is then raised. The enhancement of both wings at later times might be due to gyration of the ions in the magnetic field. Two slopes corresponding to different temperatures can be attributed to the low and high energy parts of the spectrum. Such two-temperature distributions have also been observed in linear experiments /10/. But only one side of the spectrum was observed there. The time variation of the bulk temperature T_{i1} derived from the central part of the spectrum is plotted in Fig. 12 for both initial densities. The temperature T_{i2} associated with the wings is given in Fig. 13.

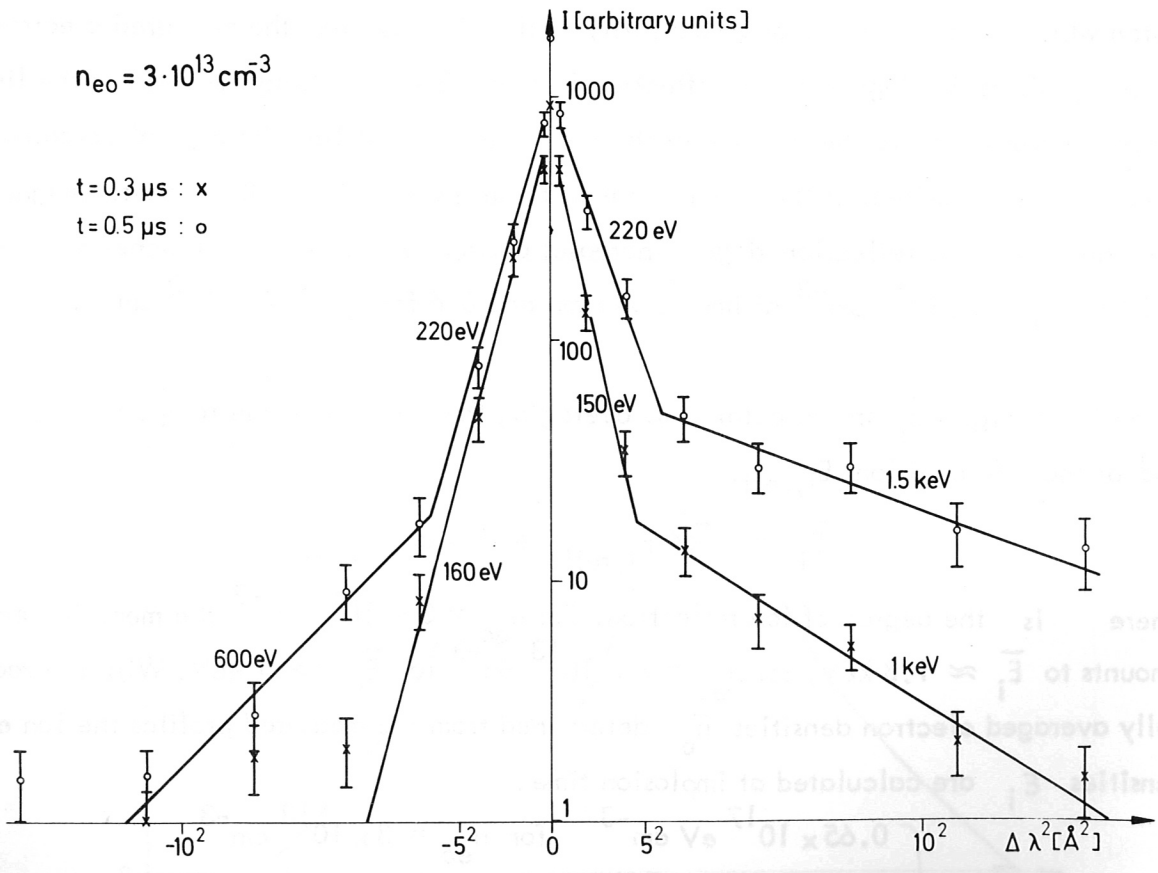

Fig. 11 D_α line profile, observed in the axial direction at $t = 0.3$ µs and $t = 0.5$ µs for $n_{eo} = 3 \times 10^{13}$ cm^{-3}

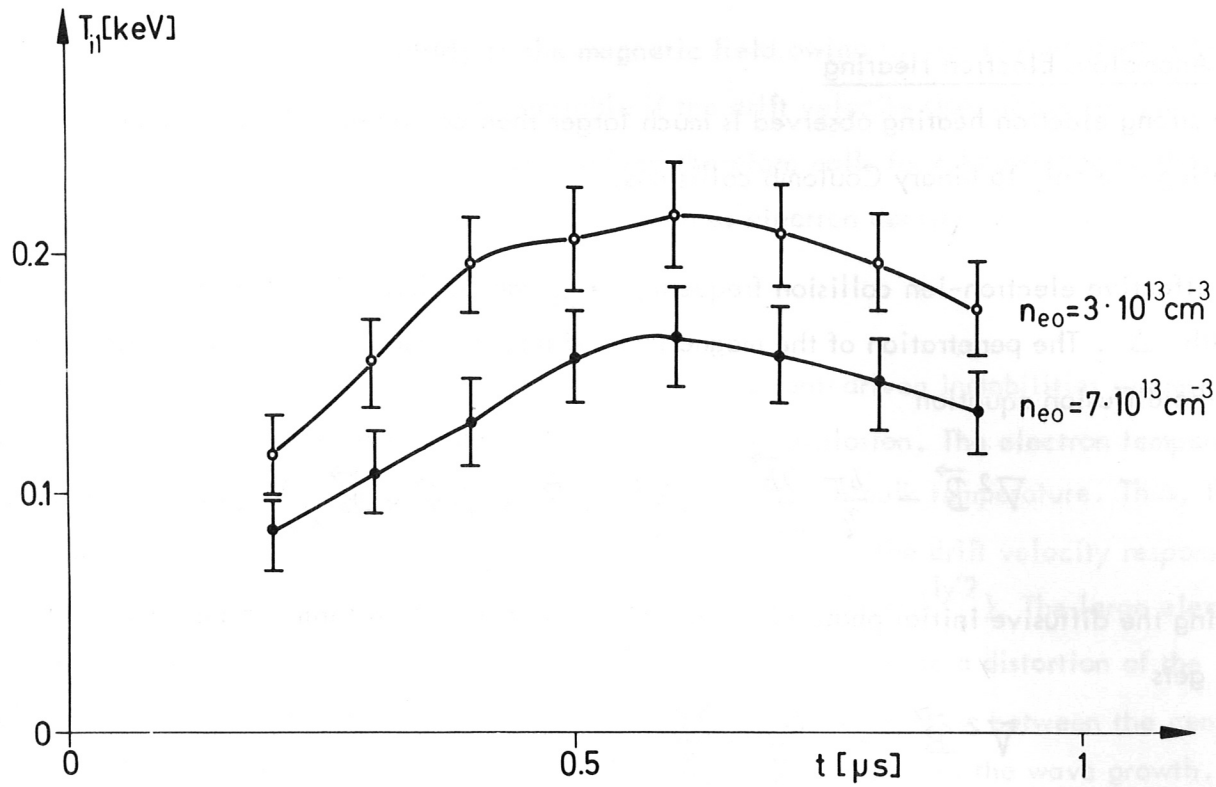

Fig. 12 Ion bulk temperature history from axial D_α line measurements for $n_{eo} = 3 \times 10^{13}$ cm^{-3} and $n_{eo} = 7 \times 10^{13}$ cm^{-3}

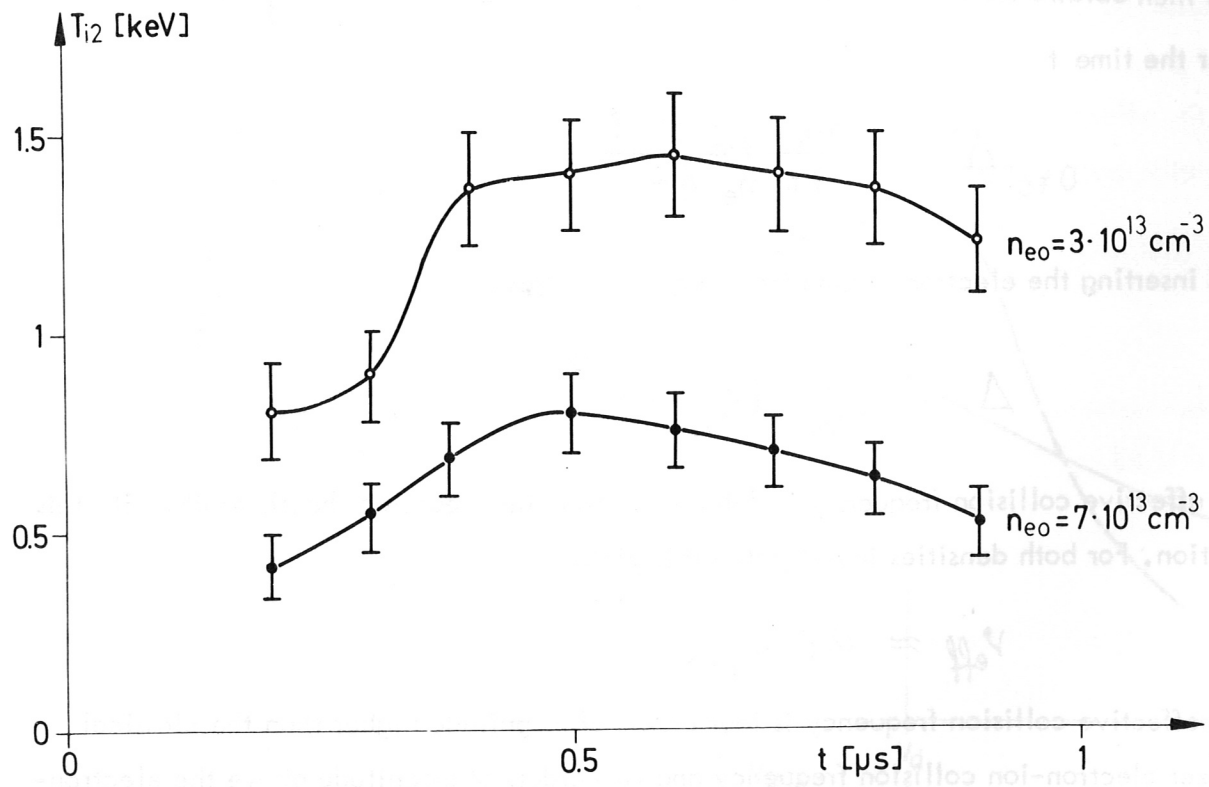

Fig. 13 Ion tail temperature history from axial D_α line measurements for $n_{eo} = 3 \times 10^{13}$ cm^{-3} and $n_{eo} = 7 \times 10^{13}$ cm^{-3}

V. Anomalous Electron Heating

The strong electron heating observed is much larger than can be explained by ohmic heating due only to binary Coulomb collisions.

An effective electron-ion collision frequency ν_{eff} can be determined from the sheath width Δ . The penetration of the magnetic field into a resistive conductor is described by the diffusion equation

$$\nabla^2 \vec{B} - \frac{4\pi}{\eta} \frac{\partial \vec{B}}{\partial t} + \frac{4\pi}{\eta} \left(\vec{\nabla} \times \left(\vec{\nabla} \times \vec{B} \right) \right) = 0$$

During the diffusive initial phase of compression, the convection term can be ignored and one gets

$$\nabla^2 \vec{B} - \frac{4\pi}{\eta} \frac{\partial \vec{B}}{\partial t} = 0$$

The resistance η is given by the effective electron-ion collision frequency ν_{eff}

$$\eta = \frac{m_e \nu_{eff} c^2}{n_e e^2}$$

One then obtains for the diffusion length Δ of the magnetic field into the plasma after the time t

$$\Delta^2 = \frac{m_e \nu_{eff} c^2 t}{4\pi n_e e^2}$$

And inserting the electron plasma frequency ω_{pe} gives

$$\Delta = \frac{c}{\omega_{pe}} (\nu_{eff} t)^{1/2}.$$

The effective collision frequency is determined from the measured sheath widths with this relation. For both densities investigated this yields

$$\nu_{eff} \approx 0.6 \, \omega_{pi,o}.$$

This effective collision frequency is four orders of magnitude higher than the classical Spitzer electron-ion collision frequency and two orders of magnitude above the electron-neutral collision frequency. The enhanced effective collision frequency may be caused by collective particle-wave interaction. Waves may be excited in the current carrying

compression sheath perpendicularly to the magnetic field owing to the relative drift between electrons and ions. These waves grow unstable if the drift velocity rises above the phase velocity. Discussion of the instabilities involved therefore calls for a knowledge of the drift velocity and the local plasma parameters such as electron density, electron temperature and ion temperature.

Considering the excitation conditions of the possible current-driven instabilities suggests that the ion sound instability should dominate during the implosion. The electron temperature in the current carrying region is large compared with the ion bulk temperature. Thus, the necessary condition for ion sound $T_e >> T_i$ holds. Further on the drift velocity responsible for wave growth has to exceed the ion sound velocity ($v_s = (T_e/m_i)^{1/2}$). The large electron density and temperature gradients observed in the experiment lead to a distortion of the electron distribution function as found by Dum /11/. The drift velocity between the centres of mass of the electron and the ion distribution then no longer governs the wave growth. But gradient drifts $v_{\nabla n_e}$, $v_{\nabla T_e}$ due to the distortion of the electron distribution have to be added to the centre of mass drift, i.e. the diamagnetic drift velocity $v_{d,i}$. The influence of these gradient drifts is clarified for the example of the temperature gradient in Fig. 14.

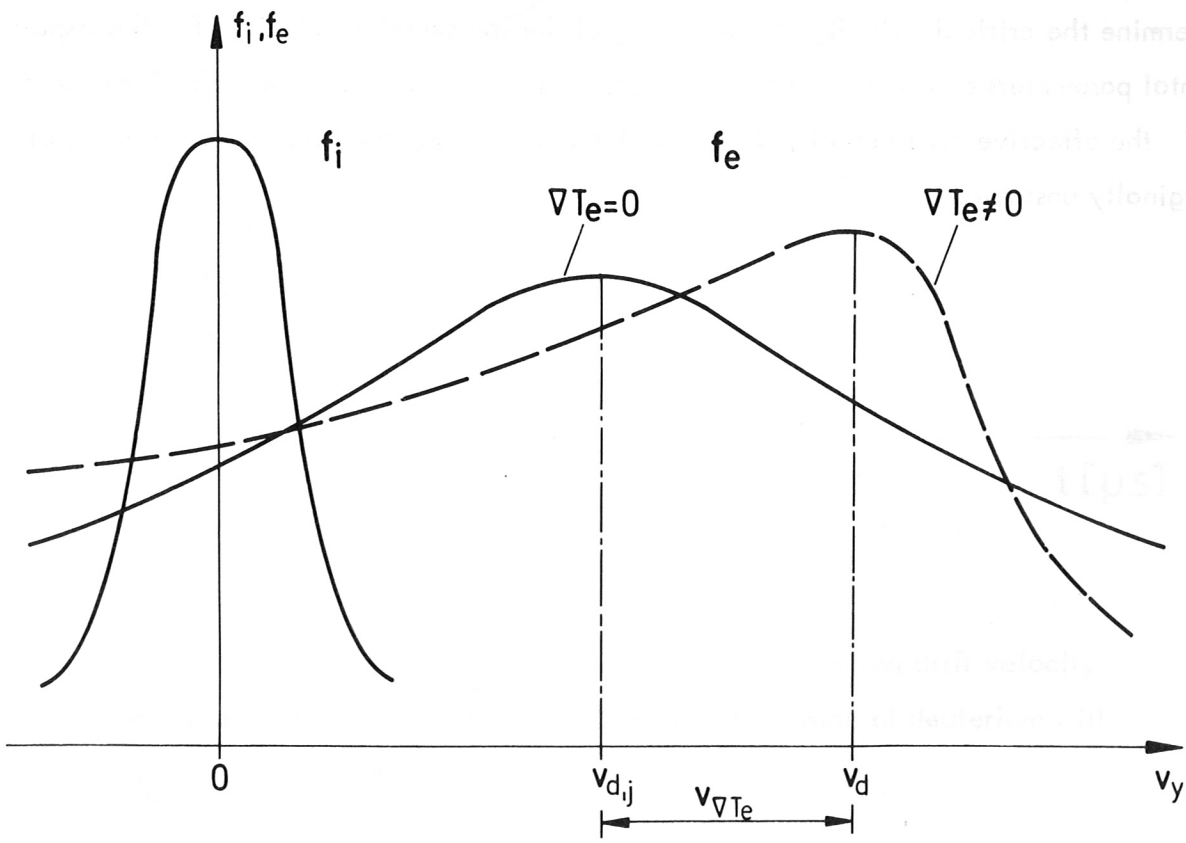

Fig. 14 Distortion of the electron distribution function f_e due to electron temperature gradient ∇T_e and the resulting additional drift velocity $v_{\nabla T_e}$ for wave growth, $v_{d,ij}$ = relative electron-ion drift velocity

In the limit $\omega_{ge} >> \nu_{eff}$ the total effective drift for wave growth then reads

$$\vec{v}_{d,eff} = \vec{v}_{d,i} + C_1 \vec{v}_{\nabla n_e} + C_2 \vec{v}_{\nabla T_e}$$

The coefficients C_1, C_2 depend on the shape of the electron distribution function. The effective drift is determined for the measured parameters of the experiment including the gradient terms in the case of ion sound turbulence /11/.

The time variation of this effective drift velocity together with those of the diamagnetic drift velocity and the ion sound velocity in the piston region is plotted in Fig. 15 for $n_{eo} = 3 \ 10^{13} \ cm^{-3}$. It shows that only the gradient terms make ion sound turbulence possible during the whole implosion phase.

Damping of the ion sound waves on the ions should produce a high energy tail in the ion distribution /12/. The parameters of the tail, i.e. number and energy of the tail ions, determine the critical velocity for quenching of the ion sound instability. For the experimental parameters obtained from the D_α measurements, this critical velocity is of the order of the effective drift velocity during implosion. The ion sound therefore remains just marginally unstable.

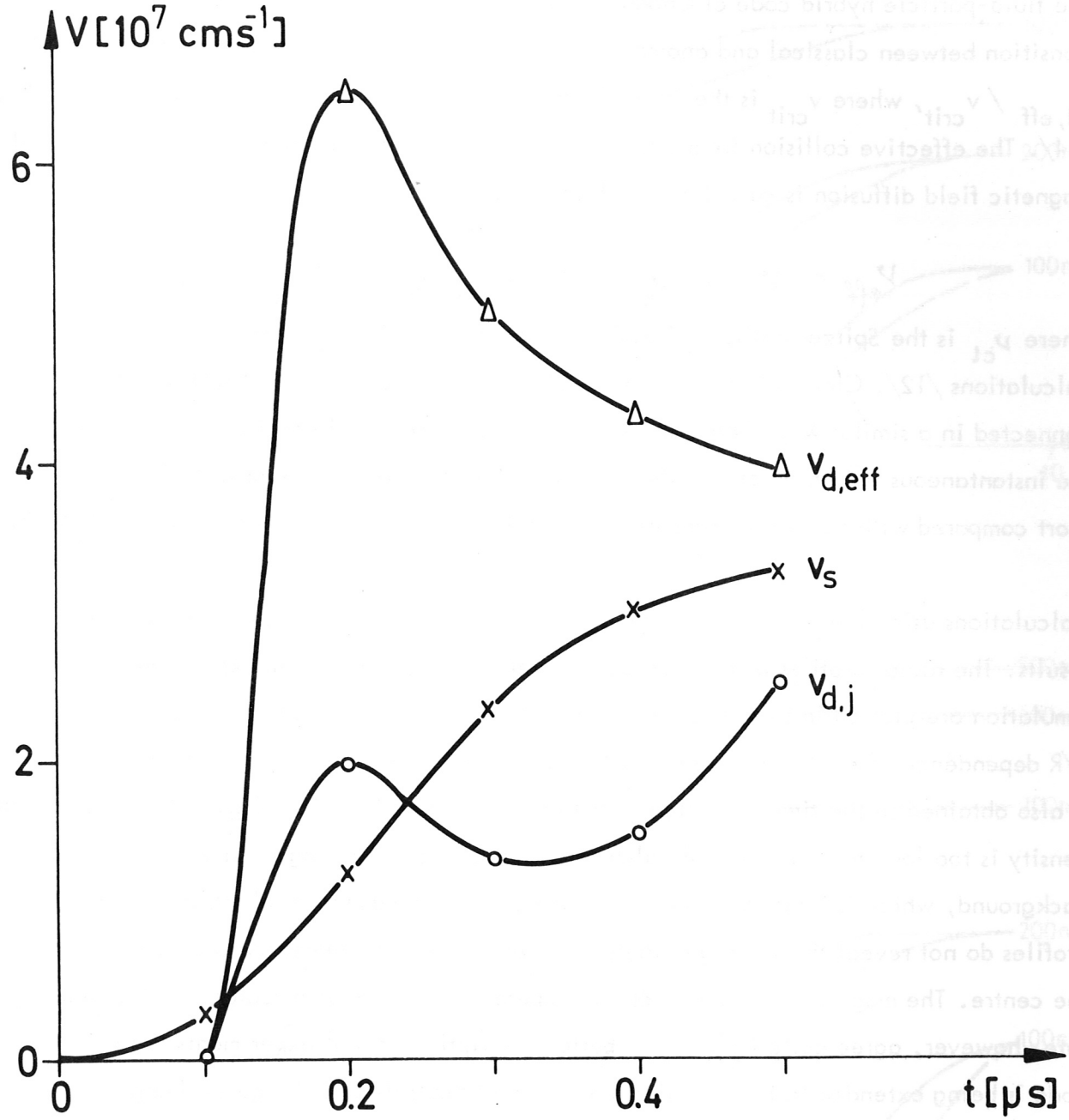

Fig. 15 The effective velocity $v_{d,eff}$, the relative electron-ion drift velocity $v_{d,i}$ and the ion sound velocity v_s during the compression of deuterium with $n_{eo} = 3 \times 10^{13}$ cm^{-3}

VI. Comparison of the Experimental Results with Hybrid Code Calculations

The fluid-particle hybrid code of Chodura /13/ has been modified to provide a continuous transition between classical and anomalous transport depending on the local ratio $v_{d,eff} / v_{crit}$, where v_{crit} is the critical drift velocity for onset of the ion sound instability /14/. The effective collision frequency for electron heating, electron heat conduction and magnetic field diffusion is calculated with the ansatz

$$\nu_{eff} = \nu_{cl} + \nu_{an} \left(1 - \exp\left(-v_{d,eff} / v_{crit}\right)^2\right),$$

where ν_{cl} is the Spitzer collision frequency and $\nu_{an} = 10^{-2}\ \omega_{pe}$ from numerical calculations /12/. Classical and anomalous electron heat conduction /15, 11/ are connected in a similar way. The fast growth of the ion acoustic instability may justify the instantaneous switch on of turbulence to its saturation value. The growth time is short compared with the transit time of the particles through the turbulent region: $\gamma t_t \approx 15$.

Calculations using the hybrid code show rather good agreement with the experimental results. The radial profiles of the toroidal magnetic field profiles from experiment and simulation are plotted in Fig. 16a, b for the two initial densities investigated. The 1/R dependence of the toroidal belt pinch field is thereby eliminated. Good agreement is also obtained in the time variation of the degree of ion reflection (Fig. 17). The electron density is too low in the numerical calculations at later times owing to lack of a neutral background, which is ionized in the experiment. Also the numerical electron temperature profiles do not reveal the steep gradients observed in the experiment but are flat towards the centre. The magnitude of the electron temperature in the piston region and the heating rate, however, agree quite well. For a better description of real experiments the hybrid code is being extended to include also ionization of neutrals and charge exchange /16/.

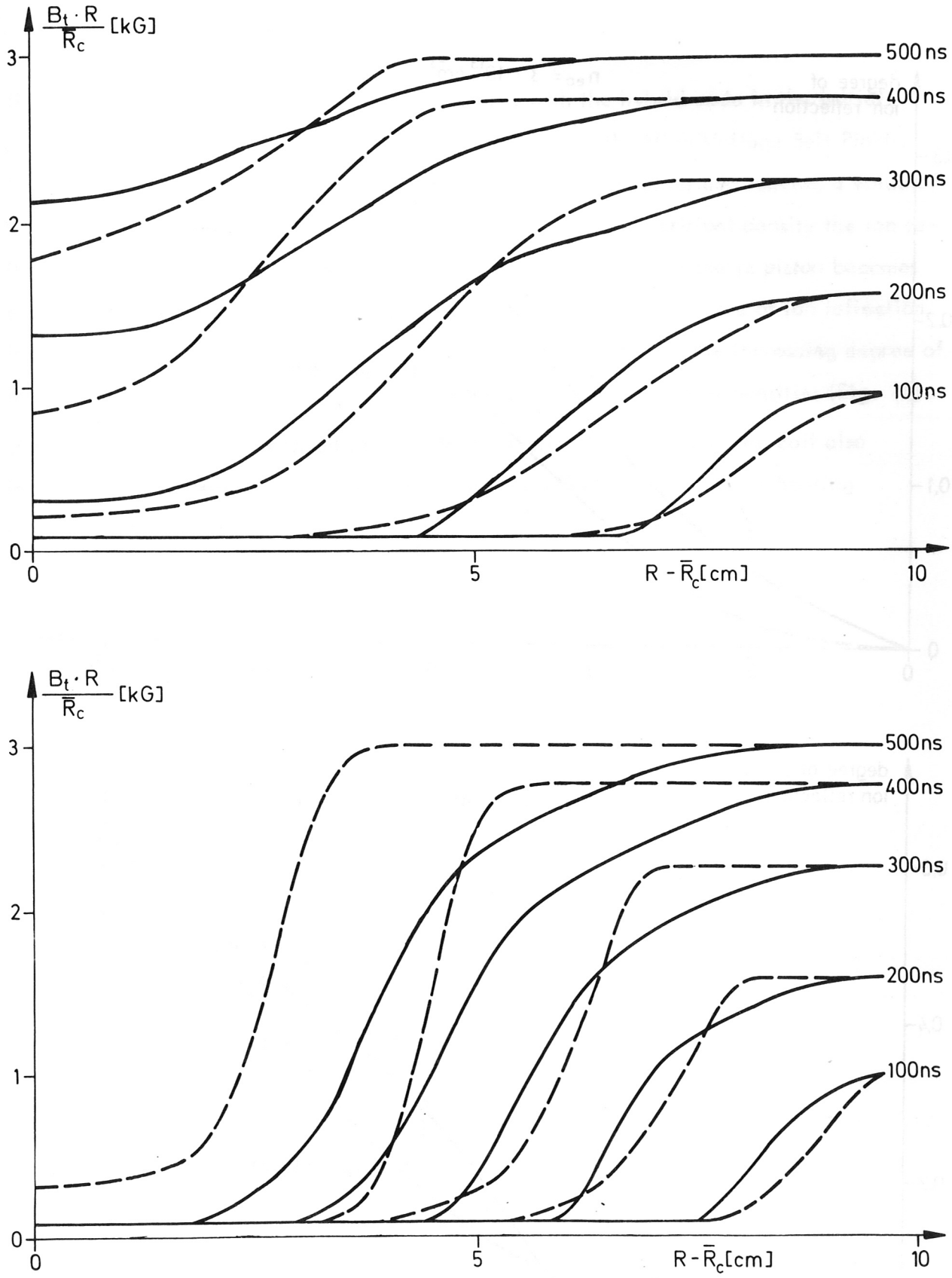

Fig. 16 Time evolution of the radial magnetic field profiles in experiment (solid curves) and code (dashed curves). The 1/R-dependence of the toroidal magnetic field B_t is eliminated by multiplying by $R/\bar{R}_c$, $\bar{R}_c$ = mean coil radius

a) $n_{eo} = 3 \times 10^{13}$ cm^{-3}

b) $n_{eo} = 7 \times 10^{13}$ cm^{-3}

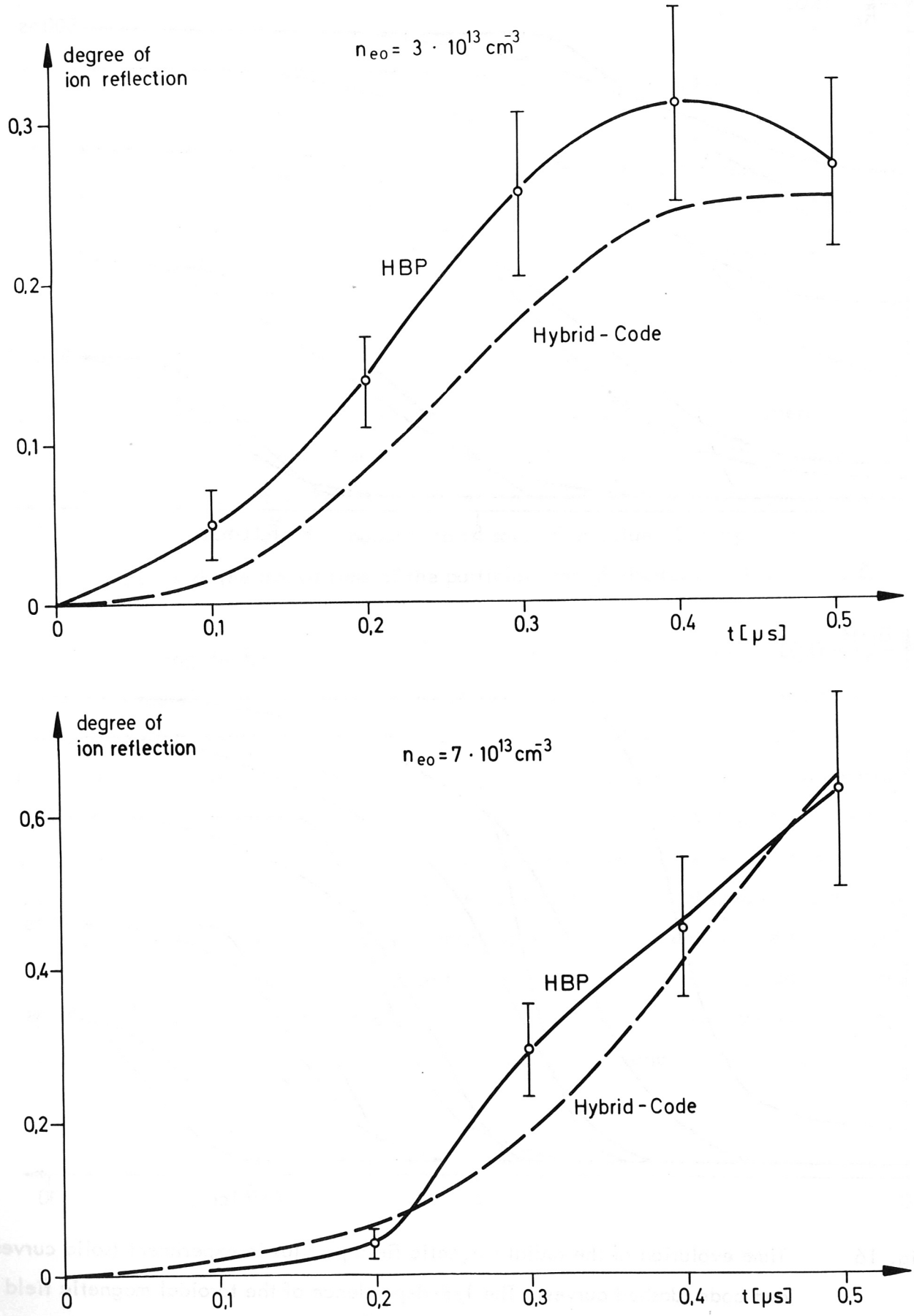

Fig. 17 Time history of degree of ion reflection in experiment (solid lines) and code (dashed lines)

The scaling of shock compression was investigated with the hybrid code in the initial density range $5 \times 10^{12} - 10^{14}$ cm^{-3} for the parameters of the High Voltage Belt Pinch. Towards lower densities the width of the magnetic piston increases and reaches a value of half the compression length at $n_{eo,c} = 9 \times 10^{12}$ cm^{-3}. At this critical density the ion reflection ceases because the transit time of the ions through the magnetic piston becomes equal to the implosion time. Towards higher initial densities the degree of ion reflection increases and amounts to 0.65 at $n_{eo} = 10^{14}$ cm^{-3}. As a result of the increasing degree of ion reflection the ion heating exceeds the electeon heating at higher densities (Fig. 18).

The total plasma energy referred to the total magnetic field energy in the coil also increases with increasing initial density. Thus, the effectiveness of shock heating increases with increasing density owing to increasing ion reflection.

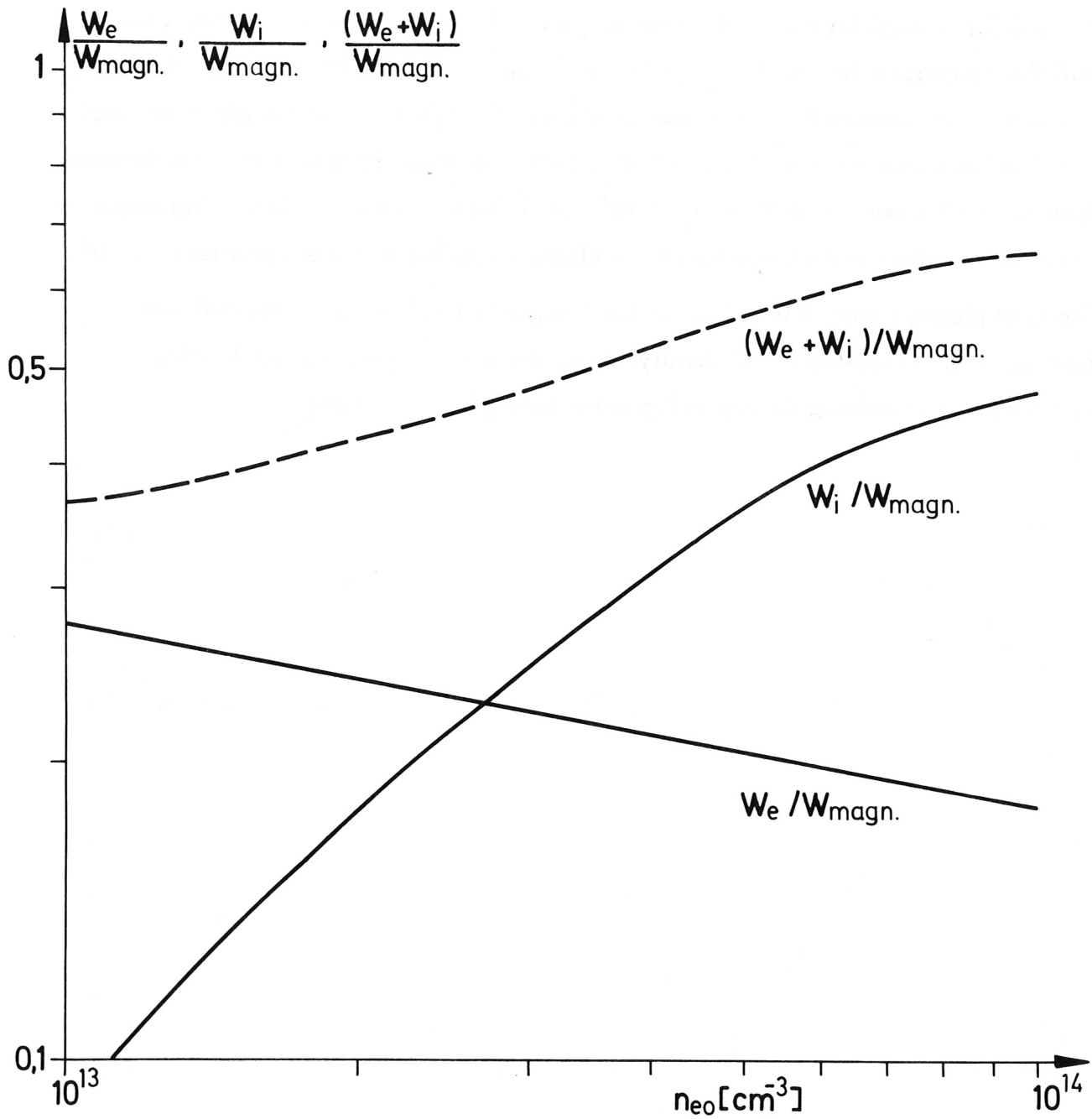

Fig. 18 Scaling of the total electron and ion energies W_e and W_i, respectively, with the initial density n_{eo} from parameter studies with the simulation code. The plasma energies are related to the total magnetic field energy in the discharge vessel W_{magn}.

VII. Conclusions

Shock heating in the High Voltage Belt Pinch results in weakly compressed high-ß plasmas with electron and ion temperatures in the keV range. The elimination of end losses in the toroidal configuration leads to higher electron temperatures that still persist after compression. The strong electron heating can be attributed to ion sound turbulence. The contribution of density and temperature gradients to the effective drift velocity for wave growth is essential for excitation of the ion acoustic instability. Damping of the ion sound waves on the ions generates a high energy ion tail. Ion heating increases with higher initial density owing to increasing ion reflection from the magnetic piston. The experimental results are well described by a fluid-particle hybrid code which includes classical and anomalous transport.

References

/1/ Fünfer, E., M. Kaufmann, W. Lotz, J. Neuhauser, G. Schramm, U. Seidel, Nucl. Fusion 15, 133 (1975)

/2/ Becker, G., Nucl. Fusion 14, 319 (1974)

/3/ McKenna, K.F., R. Kristal, K.S. Thomas, Phys. Rev. Lett.32, 409 (1974)

/4/ DeSilva, A.W., W.F. Dove, I.J. Spalding, G.C. Goldenbaum, Phys.Fluids 14, 42 (1971)

/5/ Hintz, E., 3rd IAEA Conf. on Plasma Physics and Contr. Nucl.Fusion Research, Novosibirsk, Vol.I, 69 (1968)

/6/ Keilhacker, M., M. Kornherr, H. Niedermeyer, F. Söldner, K.-H. Steuer, 6th Europ.Conf. on Contr.Fusion and Plasma Physics, Moscow, Vol. I, 303 (1973)

/7/ Keilhacker, M., M. Kornherr, G. Maret, H. Niedermeyer, K.-H. Steuer, 5th Europ. Conf. on Contr. Fusion and Plasma Physics, Grenoble, Vol. I, 47 (1972)

/8/ Chodura, R., C.T. Dum, M. Keilhacker, M. Kornherr, H. Niedermeyer, R.Protz, F. Söldner, K.-H. Steuer, 5th IAEA Conf. on Plasma Physics and Contr. Nucl.Fusion Research, Tokio, Vol. III, 397 (1974)

/9/ Protz, R.,F. Söldner, K.-H. Steuer, J.Appl.Phys. 48, 125 (1977)

/10/ Höthker, K., Nucl. Fusion 16, 253 (1976)

/11/ Dum, C.T., IPP Report 6/153, Garching (1977), to be published in Phys. Fluids

/12/ Dum, C.T., R. Chodura, D. Biskamp, Phys. Rev. Lett. 32, 1231 (1974)

/13/ Chodura, R., Nucl. Fusion 15, 55 (1975)

/14/ Stringer, T.E., J. Nucl. Energy (Pt.C) 6, 267 (1964)

/15/ Braginskii, S.I., Rev. of Plasma Physics 1, 205 (1965)

/16/ Chodura, R., C.T. Dum, F. Söldner, K.-H. Steuer, 8th Europ. Conf. on Contr. Fusion and Plasma Physics, Prag (1977)

Acknowledgements

The author would like to thank Prof. Dr. E. Fünfer for the apportunity to perform these investigations at Max-Planck-Institut für Plasmaphysik. He is especially indebted to Dr. K.-H. Steuer for his guidance and encouraging support. It is a pleasure to acknowledge the help of Dr. C.T. Dum in the theoretical interpretation and valuable discussions with Dr. R. Chodura. Thanks are due to R. Protz and W.-G. Wrobel for helpful cooperation and to F. Braum and D. Pohl for valuable technical assistance. The author would also like to thank Dr. M. Keilhacker, Dr. M. Kornherr and Dr. H. Niedermeyer, who were involved in designing the experiment.